# An analytical model for the velocity and gas fraction profiles near gas-evolving electrodes

Rajora, A.; Haverkort, J. W.

**DOI**
10.1016/j.ijhydene.2023.03.154

**Publication date**
2023

**Document Version**
Final published version

**Published in**
International Journal of Hydrogen Energy

INTERNATIONAL JOURNAL OF HYDROGEN ENERGY 48 (2023) 27450–27463

Available online at www.sciencedirect.com

ScienceDirect

journal homepage: www.elsevier.com/locate/he

# An analytical model for the velocity and gas fraction profiles near gas-evolving electrodes

*A. Rajora, J.W. Haverkort* *

*Process & Energy Department, Delft University of Technology, Leeghwaterstraat 39, 2628 CB, Delft, the Netherlands*

## HIGHLIGHTS

- Using the integral method we derive analytical relations for velocity and gas fraction profiles near a gas-evolving electrode.
- Analytical expressions for the electrolyte flow rate under natural convection conditions are obtained.
- We successfully validate our analytical results using a computational mixture model.
- For a constant bubble diameter, the gas plume thickness first decreases and then increases with increasing current density.
- At high current densities, the velocity boundary layer thickness is approximately independent of current density.

## ARTICLE INFO

*Article history:*
Received 31 January 2023
Accepted 11 March 2023
Available online 18 April 2023

*Keywords:*
Multiphase flow
Water electrolysis
Natural convection
Bubbles
Scaling analysis

## ABSTRACT

Understanding multiphase flow close to the electrode surface is crucial to the design of electrolyzers, such as alkaline water electrolyzers for the production of green hydrogen. Vertical electrodes develop a narrow gas plume near their surface. We apply the integral method to the mixture model. Considering both exponentially varying and step-function gas fraction profiles, we derive analytical relations for plume thickness, velocity profile, and gas fraction near the electrode as a function of height and current density. We verify these analytical relations with the numerical solutions obtained using two-dimensional mixture model simulations. We find that for low gas fractions, the plume thickness decreases with an increase in current density for an exponentially varying gas fraction profile. In contrast, the plume thickness increases with increasing current density at high gas fractions for an approximately step-function-shaped gas fraction profile, in agreement with experiments from the literature.



## Introduction

Many electrochemical reactions produce gaseous products with low solubility in the electrolyte. In this case, bubbles are evolved at the electrode surface, for example, in the production of aluminium [1], sodium chlorate [2], chlorine [3,4], and hydrogen using water electrolysis [5–9]. Bubbles add to the resistance of the electrochemical systems by decreasing the effective conductivity of the electrolyte [7,10–14] and by taking away the reactive electrode area [15–20]. Bubbles also induce convection in the electrolyte [21–23], increasing the mass transport of reactants and products. The efficiency of the electrochemical cell is, thus, closely related to the two-phase hydrodynamics of bubbles and the electrolyte [24,25].

* *Corresponding author.*
E-mail addresses: A.Rajora@tudelft.nl (A. Rajora), J.W.Haverkort@tudelft.nl (J.W. Haverkort).
https://doi.org/10.1016/j.ijhydene.2023.03.154

**Nomenclature**

*Dimensionless variables*

| | |
|---|---|
| $\varepsilon$ | gas fraction |
| $Pr_b$ | bubble Prandtl number |
| $q$ | $\equiv \delta_f/\delta_g$ |

*Greek variables*

| | |
|---|---|
| $\delta_f$ | flow boundary layer thickness [m] |
| $\delta_g$ | gas plume thickness [m] |
| $\nu$ | kinematic viscosity [$m^2/s$] |
| $\rho$ | liquid density [$kg/m^3$][1] |

*Subscripts and other notation*

| | |
|---|---|
| Hd | hydrodynamic diffusion |
| St | Stokes |
| g | gaseous property |
| m | mixture property |
| max | maximum value of the variable |
| min | minimum value of the variable |
| s | slip |

*Symbols*

| | |
|---|---|
| $x$ | wall normal coordinate [m] |
| $z$ | vertical coordinate [m] |
| $\langle W \rangle$ | average superficial liquid velocity [m/s] |
| $U$ | superficial velocity in the $x$ direction [m/s] |
| $\mathcal{W}$ | characteristic velocity in Eq. (8) [m/s] |
| $u$ | interstitial velocity in the $x$ direction [m/s] |
| $w$ | interstitial velocity in the $z$ direction [m/s] |
| $w'$ | strain rate at the electrode $\equiv \frac{\partial w}{\partial x}\big\vert_{x=0}$ [1/s] |
| $\mathbf{u}$ | interstitial velocity [m/s] |
| $D_b$ | bubble dispersion coefficient [$m^2/s$] |
| $d_b$ | bubble diameter [m] |
| $g$ | acceleration due to gravity [$m/s^2$] |
| $h$ | height of the electrode [m] |
| $j$ | current density [$A/m^2$] |
| $l$ | electrode-wall distance [m] |
| $P$ | reduced pressure $= p + \rho g z$ [Pa] |
| $p$ | pressure [Pa] |
| $z_{eff}$ | height at which the analytical flow rate matches the numerical flow rate [m] |

Gas-evolving electrodes are usually oriented vertically [26] to avoid bubble accumulation. Once released from the electrode surface, bubbles move primarily in a vertical direction due to their buoyancy and the resulting electrolyte flow. Their drag on the fluid induces natural convection of the electrolyte. Several hydrodynamics forces push the bubbles in the lateral direction, forming a bubble curtain or plume, as shown in Fig. 1.

The study of velocity plumes near a vertical wall has been of interest for a long time, particularly for natural convection effects [27–33]. In electrochemical applications, gas may be evolved at electrodes on two opposing surfaces, for example, in a membraneless electrolyzer [9,34–40] or only one of the two surfaces, for example, in a zero-gap electrolyzer [10,41–43] or a conventionally divided electrolyzer in which the second surface is a membrane or a diaphragm [13,44].

Previously, analytical attempts have been made to study the case of two adjacent gas-evolving electrodes resulting in two plumes on opposite walls [6,9,45,46]. Reference [47] derives a criterion for the occurrence of back-flow. In Refs. [9,45], the relations for the velocity profile and the wall shear stress are derived assuming a known gas fraction profile. While Ref. [45] used experiments to characterize the gas fraction profile, Ref. [9] performed multiple simulations to relate the plume thickness to the operating parameters. Reference [46] used a thermal analogy and dimensional analysis to predict the scaling of plume thickness with geometric and operating parameters. However, the prefactors for the scaling laws were not established due to the use of simple dimensional analysis.

In this work, we focus on a single plume, relevant for electrochemical cells where the bubbles are produced at only one electrode, when there is a membrane or diaphragm in between the electrodes, or when the two electrodes are placed far apart. We start from an integral method similar to that previously used for studying natural convection due to solutal and thermal effects [28–30,33,48]. Our model contains several features somewhat particular to the diffusion of gas bubbles- for example, the use of a constant flux boundary condition, the effect of gas fraction on viscosity and density, and the existence of a maximum gas fraction. Such a maximum gas fraction is a feature typical to the diffusion of electrolytic bubbles, owing to the volume they take up, and does not arise in the case of diffusion of heat or species. To model this, we consider a step-function gas fraction profile, in addition to the widely used exponential profile, in the integral method. Using an assumed velocity profile, modified here to take into account the effect of a finite domain, we provide analytical relations for the gas plume thickness, liquid velocity profile, and liquid flow rate as a function of the height and current density of the electrolyzer.

## Model equations

We use the laminar mixture model formulation [46,49,50] to describe the two-phase hydrodynamics in the electrochemical cell.

The liquid velocities in the $x$ and $z$ direction are denoted by $u$ and $w$, respectively and we will use a subscript 'g' to denote the gas quantities. The volume fraction of gas bubbles is denoted by $\varepsilon$ *and* capital letters are used to denote superficial velocities: $\mathbf{U} = (1-\varepsilon)\mathbf{u}$. We will use $U_g$ here, only to denote the positive horizontal superficial gas velocity at the electrode surface. The continuity equation for the gaseous phase at steady state is given by $\nabla \cdot (\varepsilon \mathbf{u}_g) = 0$, which can be integrated over a Gaussian pillbox bordering the electrode at $x = 0$ to give

$$U_g = \frac{d}{dz}\int_0^l \varepsilon w dx, \tag{1}$$

where we assumed that the slip velocity in the vertical direction $w_s \equiv w_g - w$ is negligible compared to the liquid

[1] From the gas conservation equation [9], if only hydrodynamic diffusion is present: $\mathbf{U}_m \cdot \nabla \varepsilon = \nabla \cdot (\varepsilon(1-\varepsilon)\mathbf{u}_s) = \nabla \cdot \left(g d_b^3 \mathbf{D} \nabla \varepsilon / 36\nu\right) = \nabla \cdot (D_b \mathbf{D} \nabla \varepsilon)$, so the effective diffusion coefficient in the horizontal direction can be written as $D_b = d_b w_{St}/2 = \frac{g d_b^3}{36\nu}$. Here $\mathbf{U}_m$ is the superficial mixture velocity.

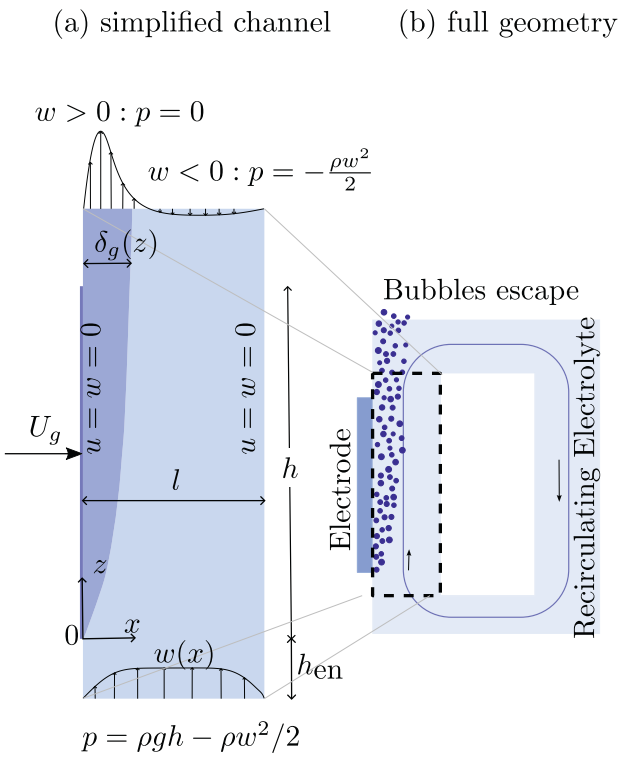


**Fig. 1 – A schematic of the gas fraction profile and velocities near a gas-evolving electrode with natural convection electrolyte recirculation. Opposite the electrode may be the membrane in a conventional configuration, or the bipolar plate or back-wall in a zero-gap configuration. The gas bubbles are generated at the electrode surface and escape from the top. The liquid electrolyte recirculates in the cell through a downcomer. We simulate only a channel geometry shown on the left. The gas bubbles are generated at the electrode surface and develop a plume of width $\delta_g$. The liquid electrolyte moves vertically with velocity $w$ (x, z). The boundary conditions used are shown adjacent to each of the boundary.**

velocity, so $w_s \ll w$. The superficial gas velocity at the electrode in the x-direction is given by Faraday's law

$$U_g = \frac{\mathcal{V}_m}{nF} j, \tag{2}$$

where $\mathcal{V}_m$ is the molar volume of the gas and $n$ is the number of electrons required to produce one gas molecule. Here we assumed that the gas evolution efficiency [51,52] is 100% so all of the produced gas is evolved as bubbles. At the surface of the electrode, $x = 0$, we can write

$$U_g = \varepsilon u_g|_{x=0} = \varepsilon u_s|_{x=0}. \tag{3}$$

For a gas density much lower than that of the liquid, $\rho_g \ll \rho$, the vertical z-component of the steady state momentum conservation equation for the gas-liquid mixture can be approximated [9] by

$$\frac{\partial(1-\varepsilon)w^2}{\partial z} + \frac{\partial(1-\varepsilon)uw}{\partial x} = -\frac{1}{\rho}\frac{\partial P}{\partial z} + \frac{\partial}{\partial x}\left(\nu_m \frac{\partial w}{\partial x}\right) + \varepsilon g, \tag{4}$$

where $P = p + \rho g z$ is the reduced pressure and $p$ is the absolute pressure. Note that in Eq. (4), we neglected the slip velocity in the vertical direction for the typically small electrochemical bubbles. This allows us to approximate the mixture velocity with the liquid velocity. The mixture kinematic viscosity $\nu_m$ can be expressed empirically using the liquid viscosity $\nu$ and gas fraction $\varepsilon$ as $\frac{\nu_m}{\nu} = \frac{1}{1-\varepsilon} \geq 1$ [47,53,54].

The model is completed by using empirical relations describing the relative velocity between the bubbles and the electrolyte. While it has been observed that the bubble size increases along the height of the electrode [2,55], we assume here a constant bubble diameter $d_b$ for simplicity. The bubble diameter may also increase with increasing current density [2], which can be easily included in the analytical model by inserting the dependence of $d_b$ on current density. The relative velocity of a bubble is mainly Stokes' rise velocity in the vertical direction, given by $\mathbf{u}_{St} = \frac{g d_b^2}{18\nu}\mathbf{e}_z$, where $\mathbf{e}_z$ is the unit vector in the vertical direction. For $d_b \gtrsim 100$ μm, Stokes's velocity should be corrected for the bubble Reynolds number as this becomes greater than 1 [56–58]. In this paper, we neglect the effect of hindrance on the freely rising bubbles. For small gas fractions, the lateral slip velocity of the bubbles is primarily due to hydrodynamic self-diffusion $\mathbf{u}_{Hd} = -\frac{g d_b^3}{36\nu}\frac{\mathbf{D}\nabla\varepsilon}{\varepsilon(1-\varepsilon)}$ [46,50]. The non-isotropic dimensionless dispersion tensor is given by $\mathbf{D} = \begin{pmatrix} 1 & 0 \\ 0 & 8 \end{pmatrix}$ [9,46,50,59] so the bubble diffusion coefficient[1] becomes

$$D_b = \frac{g d_b^3}{36\nu}, \tag{5}$$

in the horizontal direction. In the case of turbulent flow, a turbulent contribution may be added. However, this will not be a constant and it will vanish at the electrode. Also, the viscosity will be impacted by turbulence. Therefore, we limit our study to laminar conditions with a spatially constant bubble dispersion coefficient.

Mono-sized spheres have a maximum theoretical packing density of $\pi/\sqrt{18} \approx 0.74$ (Kepler's Conjecture) [60], while a maximum packing density of 0.6 has been reported for loosely packed particles [61] and decreases as the particle size decreases [62]. As the gas flux from the electrode is increased, the gas fraction tends to a maximum value [63–67]. In electrolytes, still smaller maximum values of $\varepsilon_{max} = 0.2 - 0.5$ have been found and were attributed to the observed coalescence barrier [63,68]. Electrolytic bubbles have a surface charge, leading to electrostatic repulsion between bubbles [63]. The resulting interaction force due to this coalesce inhibition may be described using the granular/frictional/solid pressure [69–72]. The additional transverse dispersion and vertical rise velocity can be used to describe maximum gas fraction in plumes. Additionally, there may be other transverse bubble interaction forces causing an *apparent* maximum gas fraction. For example, shear-induced diffusion has been shown to lead to an approximately step-function-shaped gas fraction profile [9,50,73] as well. While the exact expression will depend on the underlying mechanisms, we propose a heuristic relationship to simulate the maximum gas fraction by writing the slip velocity as

$$\mathbf{u}_s = \mathbf{u}_{St} + \frac{\mathbf{u}_{Hd}}{1 - \varepsilon/\varepsilon_{max}}. \tag{6}$$

In this expression, the slip velocity will increase primarily in the horizontal direction, in which the gas fraction gradients are largest, as the gas fraction approaches a maximum. So, the maximum gas fraction is heuristically attributed here to the additional dispersion of the bubbles. This additional slip velocity will push the bubbles away from the region of the maximum gas fraction. The overall slip velocity, however, will typically remain small because as the gas fraction approaches its maximum, $\frac{1}{1-\varepsilon/\varepsilon_{max}}$ increases, but $\nabla\varepsilon$ also reduces.

## Analytical model

We consider a vertical rectangular channel with width $l$ and height $h$ as shown in Fig. 1. The gas flows in a thin plume with a thickness $\delta_g(z)$ and the gas fraction at the electrode surface is denoted by $\varepsilon_0(z)$, where z is the vertical coordinate. We use the integral method [28–30,33,48] to find analytical relations for gas plume thickness $\delta_g$, wall gas fraction $\varepsilon_0$, flow boundary layer thickness $\delta_f$ and characteristic velocity $\mathcal{W}$ as a function of height z, and the superficial gas flux $U_g$ entering through the electrode. Educated guesses for the gas fraction and velocity profiles that satisfy the boundary conditions as a function of these parameters are inserted into the governing differential eqns. (1), (3) and (4), which we subsequently integrate from $x = 0$ to $x = l$. The resulting algebraic equations can then be solved exactly. In section 3.2, we will consider a step-function shaped gas fraction, relevant for high current densities and heights giving gas fractions close to the maximum, but first we assume an exponential variation in the gas fraction.

### *Exponential gas fraction profile*

For relatively low electrode height and low gas flux at low current density or elevated pressure, we assume that the gas fraction decreases approximately exponentially with x as

$$\varepsilon = \varepsilon_0 e^{-x/\delta_g}, \tag{7}$$

where $\delta_g$ is the gas fraction e-folding plume thickness, whose development with z is yet unknown. For the velocity profile, we take

$$w = \begin{cases} \mathcal{W}\left(1-\frac{x}{\delta_f}\right)\left(1-e^{-x/\delta_g}\right), & x < \delta_f \\ 0, & x \geq \delta_f. \end{cases} \tag{8}$$

here $\delta_g$ primarily determines the velocity gradient at the wall and the flow boundary layer thickness $\delta_f$ determines the distance over which the velocity goes to zero. Since the velocity is driven by buoyancy, it will always hold that $q \equiv \delta_f/\delta_g > 1$. For thermal convection in a semi-infinite medium, often $e^{-x/\delta_f}$ is used instead of $1 - x/\delta_f$, so no separate case $w = 0$ has to be introduced to avoid negative values. A polynomial decrease beyond the maximum is also used in literature [28–30]. In our case of finite channel width, we find from the simulations that back-flow precludes an exponential-like shape of the velocity profile. Instead, we chose a linear decrease of velocity profile for simplicity. Negative vertical velocities arise far away from the electrode as a consequence of the adverse pressure gradient in the boundary conditions shown in Fig. 1. The boundary conditions model the unavoidable pressure drops associated with fluid deceleration and give rise to this back-flow. In the analytical derivation, however, we neglect the responsible $\partial P/\partial z$ term [30]. Eq. (8) does not capture negative velocities away from the electrode in case of an adverse pressure gradient. This downflow has to be considered when estimating the total liquid flow rate. We define the ratio of the flow boundary layer thickness to the gas plume thickness as

$$q \equiv \frac{\delta_f}{\delta_g}. \tag{9}$$

Using Eq. (7) and Eq. (8) for $\partial P/\partial z = 0$ and neglecting the effect of the gas fraction on viscosity, slip velocity, and inertial terms on the left-hand side of Eq. (4) for small $\varepsilon$, we derive the following expressions (see Appendix A):

$$\delta_g = \left(\frac{\nu D_b^2 z}{g U_g}\frac{q+2}{qH(q)}\right)^{1/5}, \tag{10}$$

$$\mathcal{W} = \left(\frac{D_b g^2 U_g^2 z^3}{\nu^2}\frac{q^2}{(q+2)^2 H(q)^3}\right)^{1/5}, \tag{11}$$

$$\varepsilon_0 = \left(\frac{\nu U_g^4 z}{g D_b^3}\frac{(q+2)}{qH(q)}\right)^{1/5}, \quad \text{and} \tag{12}$$

$$w' \equiv \left.\frac{\partial w}{\partial x}\right|_{x=0} = \frac{\mathcal{W}}{\delta_g} = \left(\frac{g^3 U_g^3}{\nu^3}\frac{z^2}{D_b}\frac{q^3}{q(q+2)^3 H(q)^3}\right)^{1/5}, \tag{13}$$

where $H(q) \equiv \frac{4e^{-q}-e^{-2q}+2q-3}{4q}$. The value of $q$ can be explicitly calculated by

$$q \approx \sqrt{\frac{50\mathrm{Pr}_b}{7}}\frac{1+\sqrt{0.3\mathrm{Pr}_b}}{1+\sqrt{\mathrm{Pr}_b}}. \tag{14}$$

where the bubble Prandtl number $\mathrm{Pr}_b = \frac{\nu}{D_b}$ and $D_b$ is given by Eq. (5). Electrolytically generated bubbles typically have $d_b < 150$ μm, so $D_b < \nu$ and $\mathrm{Pr}_b > 1$ or $q > 2$. Note that $U_g$ can be replaced by the current density $j$ using Eq. (2). The above analytical results have a different prefactor but the same scalings with z and $U_g$ as those previously reported for thermal and solutal natural convection with constant flux (Neumann) boundary conditions [27–31], shown in Eq. (A.9). We see that the plume widens very slowly with height, proprtional to $z^{1/5}$, but much strongly with the bubble diameter. From Eq. (5), $D_b \propto d_b^3$, so that Eq. (10) gives $\delta_g \propto d_b^{6/5}$. From Eq. (10), we predict that the gas plume thickness decreases with increasing $U_g$ or current density $j$. This is because the velocity near the electrode increases with current density, increasing the convective effect, which decreases the plume thickness. The same is predicted in Ref. [46]. In Ref. [74], the hydrogen bubble plume thickness decreased in an alkaline electrolyte under normal gravity. However, the bubble size was found to decrease with increasing current density in this experiment, which could possibly by itself also explain this result. However, sometimes this decreasing plume thickness is not observed experimentally. Reference [75] shows an increase in gas plume thickness with increasing current density. A likely reason is that $D_b^2 \sim d_b^{6/5}$ increases more than linearly with $j$.

Note that the liquid flow rate, proportional to $\mathcal{W}\delta_g$, increases with z. In the finite domain used in the simulations, this increase has to be compensated by a downflow away from the electrode that increases in magnitude with increasing height. We will discuss in more detail how to do this in Appendix D.

The scaling $\delta_g \propto z^{1/5}$ is commonly obtained for constant flux while $z^{1/4}$ is found using a constant gas fraction, or temperature in case of thermal natural convection. As expected for simulations with constant current density, our scaling $\delta_g \propto z^{1/5}$ is actually a better fit to the simulations of Ref. [46] than the $z^{1/4}$ scaling derived there.

### *Step-function gas fraction profile*

The exponential-shaped gas fraction profile is relevant at high pressure, low current density and small heights or for very large bubble dispersion coefficients $D_b$ due to a large bubble size. Often above a certain height the gas fraction no longer decreases approximately exponentially as a maximum gas fraction is approached. From our simulations, shown later, we see that the distribution of gas fraction near the maximum gas fraction is approximately like a step-function profile:

$$\varepsilon = \begin{cases} \varepsilon_0, & x < \delta_g \\ 0, & x \geq \delta_g. \end{cases} \tag{15}$$

Note that we use the same symbol $\delta_g$ here to refer to a related but slightly different quantity as before (see Fig. 2). We restrict our analysis to a constant $\varepsilon_0 = \varepsilon_{max}$. This means that we consider a constant gas fraction with a constant flux at the electrode surface. This boundary condition does not have an analogy in thermal or solutal natural convection. Since in our simulations, the shape of the velocity profile does not change significantly when the gas fraction reaches a maximum, we use the same velocity profile as before. The assumed profiles of Eq. (8) and Eq. (15) are schematically shown in Fig. 2.

Rewriting Eq. (4) using the no-slip condition $w\,(x = 0) = 0$, $\frac{\partial P}{\partial z} = 0$, and Eq. (15), we get

$$\mathcal{W} = \frac{g\varepsilon_0\delta_g^2}{\nu_m}\frac{q}{q+2}, \tag{16}$$

where $\nu_m = \frac{\nu}{1-\varepsilon_{max}}$ is a constant. Substituting Eq. (8) and Eq. (15) in Eq. (4), integrating between $y = 0$ and $y = l$ for $\delta_g < \delta_f < l$, and using Eq. (16) gives

$$0 = \frac{2\nu_m\mathcal{W}}{q\delta_g} - \frac{d}{dz}(f(q)\delta_g\mathcal{W}^2), \tag{17}$$

where $f(q) \approx \frac{-0.5e^{-2q}+8e^{-q}+0.67(q-2.05)\left((q-1.22)^2+3.98\right)}{2q^2} - 0.34\varepsilon_0\frac{(q-0.71)^2+0.04}{2q^2}$. Note that we round off the coefficients in $f(q)$, and also subsequent expressions, to two significant digits. The dependence on $\varepsilon_0$ derives from the gas fraction dependence of inertial terms in Eq. (4). Finally, Eq. (1) can be rewritten as

$$U_g z = h(q)\delta_g\varepsilon_0\mathcal{W}, \tag{18}$$

where $h(q) = \frac{1+(2q-4)e^{-1}}{2q}$. We wish to find the scalings of the relevant quantities with a power of z, similar to Eqs. 10–13.

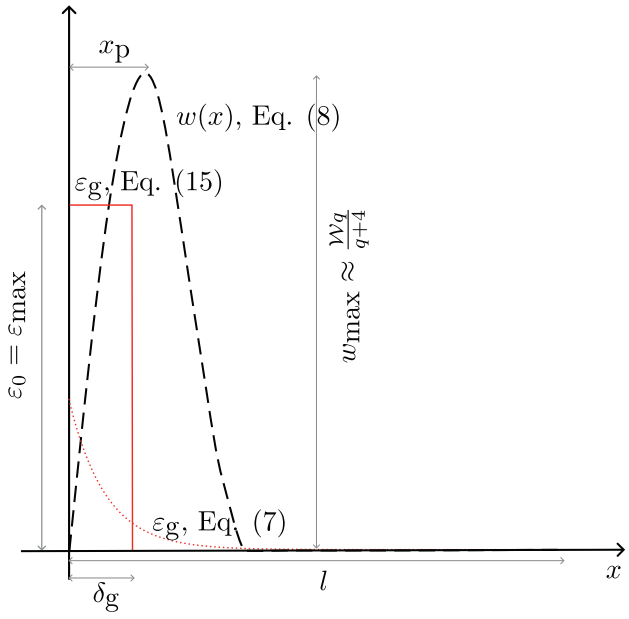


**Fig. 2 – The assumed gas fraction profile (Dotted: exponentially varying, Solid: step-function) and the assumed velocity profile (dashed: Eq. (8)). The peak velocity $w_{max} \approx \frac{\mathcal{W}q}{q+4}$ occurs at $x_p = \delta_g(q + 1 - \text{LambertW}(e^{q+1}))$, where $\text{LambertW}(x)e^{\text{LambertW}(x)} = x$. The approximation of $w_{max}$ is obtained from the asymptomatic matching of the exact expression $w\,(x_p)$ and has a maximum error of only 3%.**

Therefore, we express Eqs. 16–18 as power law expressions in $q$ so

$$\mathcal{W} = q^a\frac{g\varepsilon_0\delta_g^2}{3\nu_m}, \tag{19}$$

$$0 = \frac{2\nu_m\mathcal{W}}{q\delta_g} - f(1)\frac{d}{dz}(q^{b+1}\delta_g\mathcal{W}^2), \tag{20}$$

$$U_g z = h(1)q^c\delta_g\varepsilon_0\mathcal{W}, \tag{21}$$

where $a \equiv \frac{\ln\left(\frac{3q}{q+2}\right)}{\ln(q)}$, $b \equiv \frac{\ln\left(\frac{f(q)}{qf(1)}\right)}{\ln(q)}$ and $c \equiv \frac{\ln\left(\frac{h(q)}{h(1)}\right)}{\ln(q)}$. Assuming that $q$, $\delta_g$ $\mathcal{W}$ are proportional to some power of z, Eqs. 19–21 give $q \propto z^m$, $\mathcal{W} \propto z^{\frac{2}{3}+m\frac{a-2c}{3}}$ and $\delta_g \propto z^{\frac{1}{3}-m\frac{a+c}{3}}$ with

$$m = -\frac{1}{6+3b-4c-a} = \frac{\ln(q)}{\ln\left(\frac{3f(1)^3h(q)^4}{q^2(q+2)f(q)^3h(1)^4}\right)}, \tag{22}$$

where we used the definitions of $a$, $b$, and $c$ in the final expression. Since $a$, $b$ and $c$ vanish as $q \to \infty$, $m = -1/6$ in this limit. Inserting the scalings for $q$, $\mathcal{W}$, and $\delta_g$, Eq. (20) can be rewritten as

$$q^{b+2}\delta_g^2\mathcal{W} = \frac{2\nu_m}{kf(1)}z. \tag{23}$$

here $k = (b+1)m + \frac{1}{3} - \frac{m}{3}(a+c) + \frac{4}{3} + \frac{2m}{3}(a-2c)$ and lies between 1.43 and 1.73, using Eq. (22). Therefore, we choose a constant value, $k = 1.54$, with a maximum relative error of 12% to

simplify Eq. (23). Eliminating $\mathcal{W}$ and $\delta_g$, we can solve Eq. (19), Eq. (21), and Eq. (23) for $q$ to give

$$q = \left(\frac{\bar{z}}{\bar{z}_c}\right)^m, \tag{24}$$

where

$$\bar{z} \equiv \frac{zU_g^4}{g\varepsilon_0^5\nu_m^2}, \quad \text{and} \quad \bar{z}_c \equiv \frac{0.73h(1)^4}{f(1)^3} \approx \frac{24}{(1-\varepsilon_0)^3}. \tag{25}$$

Equation (24) is implicit since $m$ itself is a function of $q$, as given by Eq. (22). Combining Eq. (22) and Eq. (24) gives

$$\frac{2.2h(q)^4}{q^2(q+2)f(q)^3} = \bar{z}. \tag{26}$$

A good approximation, obtained by trial-and-error, to the solution of Eq. (26) is given by

$$q \approx \begin{cases} \bar{z}^{-1/6}, & \bar{z} \le 10^{-9} \\ 1.65\bar{z}^{-1/7}, & 10^{-9} < \bar{z} \le 10^{-4} \\ (\bar{z}/\bar{z}_c)^{-\frac{(1-\varepsilon_0)^{1/4}}{7}}, & 10^{-4} < \bar{z} \le \bar{z}_c \end{cases}. \tag{27}$$

The power $m = -(1-\varepsilon_0)^{1/4}/7$ in the last approximation depends weakly on $\varepsilon_0$ and varies between $-0.11$ and $-0.14$ for $\varepsilon_0 = 0.7$ and $\varepsilon_0 = 0$, respectively. Eq. (26) or (27) can be used to obtain the value of $q$. As $\bar{z} \to \bar{z}_c$, $q \to 1$. The first two approximations in Eq. (27) have a maximum error of 5% for the respective ranges of $\bar{z}$, while the last expression has a maximum error of 12% for the given range of $\bar{z}$.

Finally, $\delta_g$ solving Eq. (19) and Eq. (21) gives

$$\delta_g = \left(\frac{\nu_m U_g z(q+2)}{g\varepsilon_0^2 q h(q)}\right)^{1/3}, \tag{28}$$

$$\mathcal{W} = \left(\frac{gU_g^2 z^2 q}{\nu_m \varepsilon_0 (q+2)h(q)^2}\right)^{1/3}. \tag{29}$$

where $q$ is given by Eq. (26). We can write in the limit $q \gg 1$:

$$\delta_g = \left(\frac{e\nu_m U_g z}{\varepsilon_0^2 g}\right)^{1/3} \quad \text{and} \quad \mathcal{W} = \left(\frac{e^2 g U_g^2 z^2}{\nu_m \varepsilon_0}\right)^{1/3}. \tag{30}$$

and for the limit $q \to 1$, derived in Appendix C:

$$\delta_g = \frac{2.83\nu_m^{0.13} U_g^{0.73} z^{0.43}}{g^{0.43}\varepsilon_0^{1.17}\bar{z}_c^{0.10}} \quad \text{and} \quad \mathcal{W} = \frac{2.67 g^{0.21} U_g^{1.15} z^{0.79}}{\nu_m^{0.55}\varepsilon_0^{0.93}\bar{z}_c^{0.12}}. \tag{31}$$

where we used the last approximation in Eq. (27), evaluated at $\varepsilon_0 = 0.4$.

For $\delta_g$, the scaling with height changes from $z^{1/5}$ for an exponential plume, at small heights, to $z^{1/3} - z^{0.43}$ for a step-function gas fraction profile, at large heights. The plume thickness, thus, increases much faster with z as the height increases. The plumes are exponential for very low current densities and $\delta_g \propto U_g^{-1/5}$, see Eq. (10). As the current density increases and a maximum wall gas fraction is approached, the step-function gas fraction profile results in the scaling of $\delta_g$ between $U_g^{1/3} - U_g^{0.73}$, see Eqs. (30) and (31).

The dependence of velocity $\mathcal{W}$ on height increases from $z^{3/5}$ for an exponential plume to $z^{2/3} - z^{0.79}$ for a step-function gas fraction profile. The scaling for $\mathcal{W}$ with current density changes from $U_g^{2/5}$ at low current densities to $U_g^{2/3}$ at higher current densities when the gas fraction approaches a maximum. For the higher current densities, this dependence becomes approximately linear, $U_g^{1.15}$, according to Eq. (31). The velocity thus also increases much faster with increasing current density.

In electrolyzers, the wall strain rate is often a quantity of interest, for example, to estimate heat and mass transfer to the electrode. The wall strain rate also has an effect on the removal of bubbles attached to the surface. From Eqs. (29) and (28), we can estimate the wall strain rate $w' \equiv \frac{\partial w}{\partial x}\big|_{x=0}$ as

$$w' = \frac{\mathcal{W}}{\delta_g} = \left(\frac{g^2 U_g z \varepsilon_0 q^2}{\nu_m^2 (q+2)^2 h(q)}\right)^{1/3}. \tag{32}$$

which gives, as shown in Appendix C:

$$w' = \begin{cases} 6.4(\varepsilon_0 U_g z \nu_m^{-1})^{1/3}, & q \gg 1 \\ 3.9(1-\varepsilon_0)^{0.06}\varepsilon_0^{0.24} U_g^{0.41} z^{0.35} \nu_m^{-0.70}, & q \to 1 \end{cases}. \tag{33}$$

Interestingly, the expression for $w'$ has a minimum power of $U_g$ and z near $q \sim 5$. This is because even though the powers of $U_g$ and z in the expression of $\delta_g$ and $\mathcal{W}$ increase as the height and the current density increase, the powers in $\delta_g$ increase faster than the powers in $\mathcal{W}$ for $q < 5$. For $q > 5$, the powers of $U_g$ and z in $\delta_g$ increases slower than in $\mathcal{W}$. For $q \sim 5$, we find in Appendix C

$$w' = 4.8(1-\varepsilon_0)^{0.05}\varepsilon_0^{0.42} U_g^{0.27} z^{0.31} \nu_m^{-0.63}. \tag{34}$$

From Eqs. (32)–(34), we find that the scaling for $w'$ changes from $U_g^{3/5}$ for an exponential gas fraction profile to $U_g^{0.27} - U_g^{0.41}$ for a step-function gas fraction profile.

Another important quantity for electrolyzers is the liquid flow rate. We can calculate the average superficial liquid velocity, $\langle W \rangle = \frac{1}{l}\int_0^l w(1-\varepsilon)dx$, to be

$$\langle W \rangle = \frac{U_g z}{\varepsilon_0 l} \frac{1 + (q-1)^2 - 2e^{-q} - 2e^{-1}\varepsilon_0(q-0.64)}{2qh(q)}, \tag{35}$$

where $q$ is calculated at an effective height $z_{eff}$ for which the actual average velocity between $\delta_f$ and $l$ is negligible. Since we assumed $\partial P/\partial z = 0$ and did not consider any boundary condition for large x we effectively considered a semi-infinite domain in our analysis. In our simulations and in practice, there will usually be an opposing wall and a slight adverse pressure gradient $\partial P/\partial z$, causing some backflow $w < 0$ beyond the plume region, which is neglected in Eq. (35). In Appendix D, simulations show that a good approximation for the superficial velocity is obtained by evaluating Eq. (35) at $z = z_{eff} \sim h/3$ may be used as a rough approximation for relatively wide channels.

It should be noted that while deriving the results for the step-function gas fraction profile, the diffusion equation is not

used. As such, these relations will be valid as long as we have an approximately step-function gas fraction profile with constant $\varepsilon_0$, irrespective of the mechanism of transverse bubble transport.

## Verification using numerical solutions

We solve the mixture model formulation for multiphase flow [9,46,49,50] using COMSOL Multiphysics v5.6, update 2 [76]. The physical properties of the electrolyzer used for the simulations are listed in Table 1. We consider an electrolyzer setup as shown in Fig. 1. The gas is generated at the electrode on the left and escapes from the top boundary. The liquid electrolyte is recirculated back into the electrode channel through a downcomer section. We simulate only the electrode channel as shown in Fig. 1. This requires proper boundary conditions at the top and the bottom of the channel.

### *Boundary conditions*

The mixture model allows only the mixture and gas boundary conditions. At the electrode surface, we want to prescribe a no-slip condition for liquid and the gas flux. In the horizontal direction at the electrode surface, we use an inlet boundary condition such that the gas flux is equal to $U_g$. In the vertical direction, we impose a zero mixture velocity with zero slip velocity at the boundary nodes. This ensures that a no-slip boundary condition is imposed for the liquid phase. At the opposite boundary, we use a no-slip condition at the boundary nodes with zero mixture velocity. When the flow at the top is in the positive z − direction, a pressure boundary condition ($p = 0$) is used with gas escaping from the top boundary. When the flow at the top is in the negative z − direction, we specify a local Bernoulli condition $p = -\frac{\rho w^2}{2}$ with no gas recirculating back into the channel. At the bottom, we specify a local Bernoulli condition $p = \rho g h - \frac{\rho w^2}{2}$ with no gas flux. The boundary conditions are also shown in Fig. 1. Similar boundary conditions have been previously used for modeling natural thermal convection [77–79]. We compared the results obtained using these boundary conditions with the simulation of the full configuration of Fig. 1 in Appendix B. Using these boundary conditions, we get the results almost indistinguishable from those in the full configuration, and we could achieve faster and easier convergence of numerical results at larger heights.

**Table 1 – Dimensions and operating conditions used in numerical simulations for verification cases.**

| Properties | Value |
|---|---|
| Channel Width, $l$ | 10 mm |
| Entrance height, $h_{en}$ | 50 mm |
| Exit height, $h_{exit}$ | 50 mm |
| Electrode height, $h$ | 900 mm |
| Electrolyte density, $\rho$ | 1000 kg/m$^3$ |
| Kinematic viscosity, $\nu$ | $10^{-6}$ m$^2$/s |
| Bubble Diameter, $d_b$ | 75 μm |
| Maximum gas fraction, $\varepsilon_{max}$ | 0.4 |

### *Verification of step-function gas fraction profile relations*

We verify our analytical expressions by comparing them with various numerical results obtained using COMSOL. The numerical plume thickness is calculated by $\delta_{g,n} = \int_0^l \varepsilon dx/\varepsilon_0$ and the numerical value of the characteristic velocity $\mathcal{W}_n$ is calculated by $\mathcal{W}_n = w'_n \delta_{g,n}$. We consider different cases involving different current densities, electrode heights, maximum gas fractions, and bubble diameters. All these simulation results are obtained using the properties listed in Table 1.

Fig. 3 and Fig. 4 show the development of the gas fraction profile and the velocity profile as a function of height for $U_g = 1$ mm/s with a maximum gas fraction $\varepsilon_{max} = 0.4$. This corresponds to a current density of 8 kA/m$^2$ at atmospheric conditions for hydrogen evolution and is a representative case for the step-function gas function profile. Under some simulated conditions, a degree of turbulence can arise in actuality, which is not included in the simulations. Therefore, these

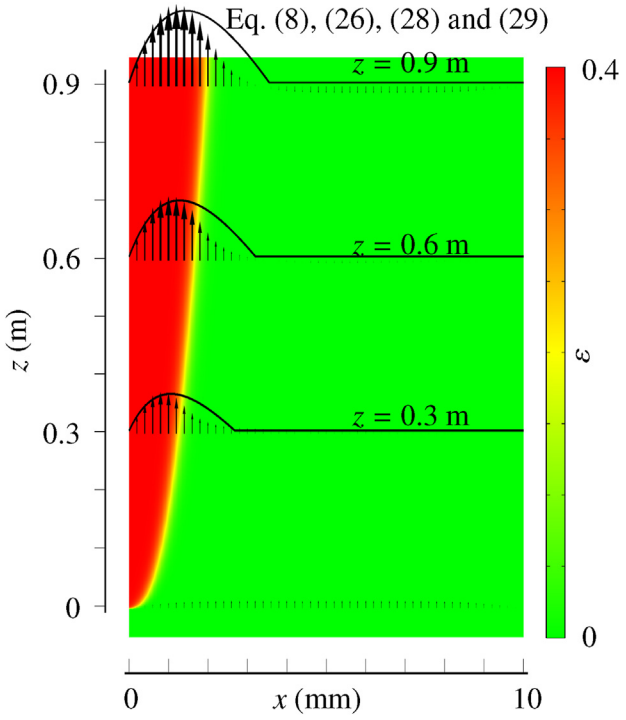


**Fig. 3 – The development of gas fraction profile and the velocity profile for the step-function gas fraction profile at $U_g = 1$ mm/s for the properties used in Table 1. The gas fraction profile is shown in color, and the numerical velocity profile is overlaid as an arrow plot at z = 0.3 m, z = 0.6 m and z = 0.9 m. The solid lines show the analytical velocity profile given by Eq. (8) at the same heights. We used Eqs. (28) and (29) to determine $\delta_f = q\delta_g$ and $\mathcal{W}$, after solving Eq. (26) numerically for $q$. (For interpretation of the references to color in this figure legend, the reader is referred to the Web version of this article.)**

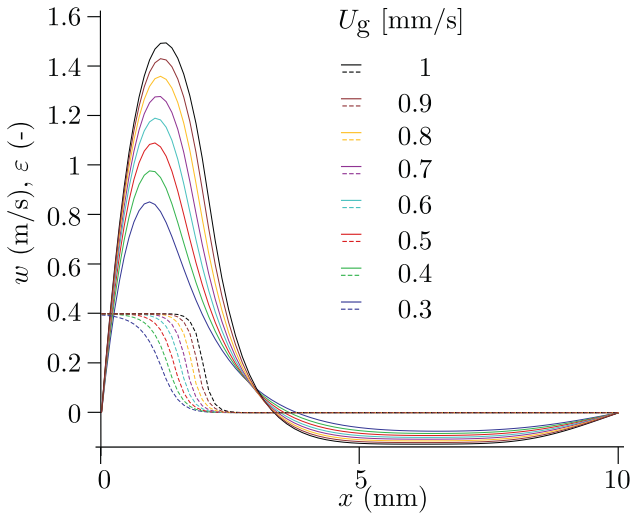


**Fig. 4 – Numerical results for gas fraction profiles (dashed) and the velocity profiles (solid) at different current densities at $z = 0.9$ m for the properties listed in Table 1. Here, the gas fraction at the electrode surface approaches a maximum value, and we see that the plume thickness, peak velocity and strain rate increase with increasing current density.**

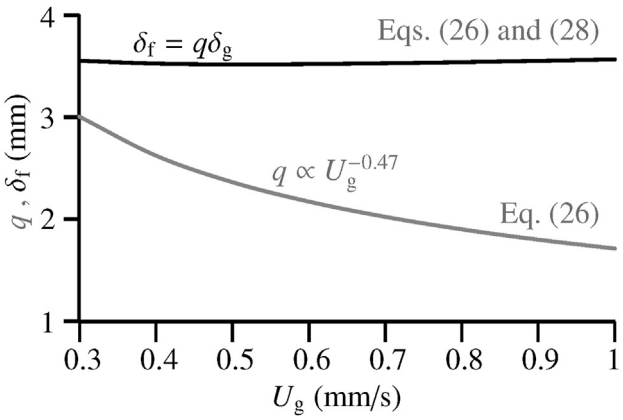


**Fig. 5 – Plot showing in our analytical model, the variation of $q$ and $\delta_f$ with $U_g$ at $z = 0.9$ m and a relatively high current density at which a step-function can approximate the gas fraction profile. While $q$ decreases, $\delta_f$ remains relatively constant. This causes all velocity profiles to cross the same point around $x = 3$ mm in. The power $q \propto U^{-0.47}$ is obtained using a least squares fit on the analytical results of Eq. (26). It is close to the power of $U_g^{-4(1-\varepsilon_0)^{1/4}/7}$ predicted by the last approximation in Eq. (27), which gives $U_g^{-0.5}$ for $\varepsilon_0 = 0.4$.**

results should be used with caution. We see an increasing plume thickness and peak velocity as the height increases. We also see that the gas fraction remains close to the maximum gas fraction and drops quickly to 0 near the edge of the plume, justifying our assumption of a step-function gas fraction profile. Interestingly, Fig. 4 shows that the velocity profiles all cross in the same point around $x \approx 3$ mm, indicating that $\delta_f$ should be approximately independent of $U_g$ in this range. This implies that while $\delta_g$ increases with increasing $U_g$, $q$ decreases, so that $\delta_f = q\delta_g$ does not change. This is also indeed predicted by our analytical solution, as shown in Fig. 5.

The characteristic velocity $\mathcal{W}$, gas plume thickness $\delta_g$, and strain rate $w'$ as a function of height are shown in Fig. 6. We see that the analytical results obtained using Eq. 29–32 show a reasonably good agreement with the numerical results obtained using COMSOL. The dotted lines show the analytical results when $q$ is calculated using Eq. (26).

In Fig. 7, we show $\mathcal{W}$, $\delta_g$ and $w'$ as a function of $U_g$ at a height of 0.9 m for the properties listed in Table 1. Due to the large range of $U_g$, we see a transition in scalings for all quantities. At small values of $U_g$, the results for the exponential-shaped gas fraction profile are valid, so $\mathcal{W} \propto U_g^{2/5}$, $\delta_g \propto U_g^{-1/5}$ and $w' \propto U_g^{3/5}$. In contrast, the results for step-function gas fraction profiles are valid at large values of $U_g$ and we find, from a least squares fit of the numerical results, that $\mathcal{W} \propto U_g^{0.68}$, $\delta_g \propto U_g^{0.42}$ and $w' \propto U_g^{0.26}$. To obtain these scaling analytically, we first calculate $q$ by using Eq. (14) for the exponential profile or by numerically solving Eq. (26) for the step-function profile. Once the value of $q$ is known, we use Eqs. (10), (11) and (13) for the exponential profile, while Eqs. (28), (29) and (32) are used for the step-function gas fraction profile. We see a good agreement with the numerical results and that the analytical results capture the transition very well. The small offset in the predicted values may be due to the discrepancy in the assumed and actual profiles, also seen in Fig. 3.

Reference [80] observes that $w' \propto U_g^{0.64}$ for oxygen bubbles and $w' \propto U_g^{0.43}$ for hydrogen bubbles for a current density range of 0.005–0.11 A/cm$^2$. In alkaline electrolytes, oxygen bubbles are substantially larger than hydrogen bubbles [74]. Therefore, it is plausible that the oxygen gas fraction profile was approximately exponential, while the hydrogen gas fraction profile was more similar to a step function. The scaling $w' \propto U_g^{0.64}$, observed for oxygen bubbles in Ref. [80] is in agreement with $U_g^{3/5}$ derived for the exponential gas fraction profile. While the scaling $w' \propto U_g^{0.43}$ for hydrogen bubbles lies close to the range $U_g^{1/3} - U_g^{0.41}$ derived in Eq. (33) for the step-function gas fraction profile.

In Fig. 7, we observe a transition from a higher power ($w' \propto U_g^{3/5}$) to a lower power ($w' \propto U_g^{0.26}$) around $U_g \approx 0.08$ mm/s or 800 A/m$^2$, see Eq. (A.6). A similar transition from a higher power at current densities around 50 A/m$^2$ to the mentioned $w' \propto U_g^{0.43}$ was observed for hydrogen. The transition from an exponential to step-function gas fraction profile could therefore be an explanation of the increasing slope of $w'$ with $U_g$ observed in Ref. [80], particularly for hydrogen bubbles, even though there is a lot of scatter in the experimental data at low

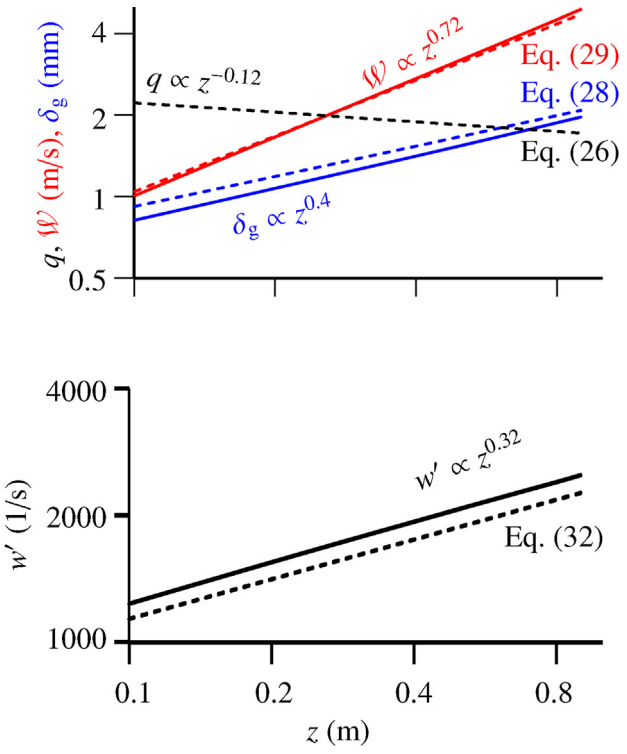


**Fig. 6 – Log-log plot of $\mathcal{W}$, plume thickness $\delta_g$, and wall shear rate $w'$ as a function of height z for $U_g = 1$ mm/s using the properties listed in Table 1. It can be seen that the analytical results (dashed line) have a reasonably good agreement with the numerical results (solid line). There are small differences in the magnitude, possibly due to the discrepancy in the assumed velocity and gas fraction profiles. We used Eq. (26) to numerically solve for $q$ and found that it decreases as the height increases, highlighted explicitly in Eq. (27).**

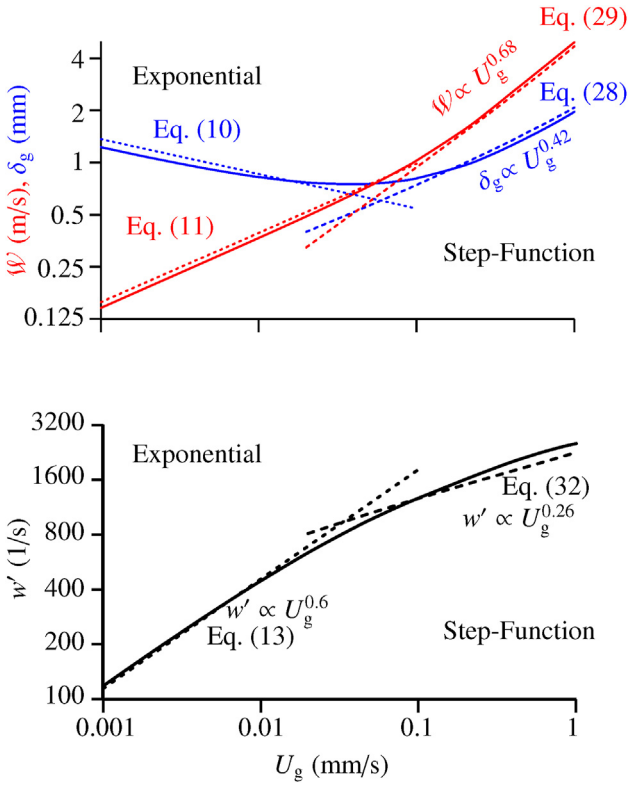


**Fig. 7 – Log-log plot of $\mathcal{W}$, plume thickness $\delta_g$, and shear rate $w'$ with $U_g$ at $z = 0.9$ m using the properties in Table 1. The solid line represents the numerical solution using COMSOL while the dashed lines correspond to our analytical solution. Here, we used Eq. (26) to solve for $q$ numerically. We see a transition from an exponential gas fraction profile to a step-function gas fraction profile, evident from the change of slope. For a hydrogen evolution reaction, $U_g = 1$ mm/s corresponds to a current density of 8 kA/m$^2$ at atmospheric conditions.**

current density. The step-function gas fraction profile analysis will be relevant for many experimental results with small bubbles. For bigger bubbles, the exponential gas profile analysis may be more appropriate.

In Fig. 8, we show the natural convection electrolyte flow rate as a function of the superficial gas flux. We see that the flow rate increases as the gas flux is increased due to the presence of a larger amount of bubbles, resulting in increased buoyancy. We also see that Eq. (35) predicts the numerical results with good accuracy using $z = 0.4h$, in agreement with Fig. D.11 for $l = 10$ mm.

For the verification of our step-function gas fraction profile results in Figs. 3–8, we used a fixed bubble diameter of 75 μm and a maximum gas fraction of 0.4. We also verified our results at a smaller bubble diameter of 50 μm and different maximum gas fractions of 0.3, 0.4, and 0.5. We used a smaller $U_g = 0.2$ mm/s, as the maximum gas fraction is reached earlier for smaller bubble diameters due to the associated lower bubble dispersion coefficient. We summarize these results in Table 2 for $z = 0.9$ m. We see again a good agreement of analytical results with the numerical results obtained using COMSOL.

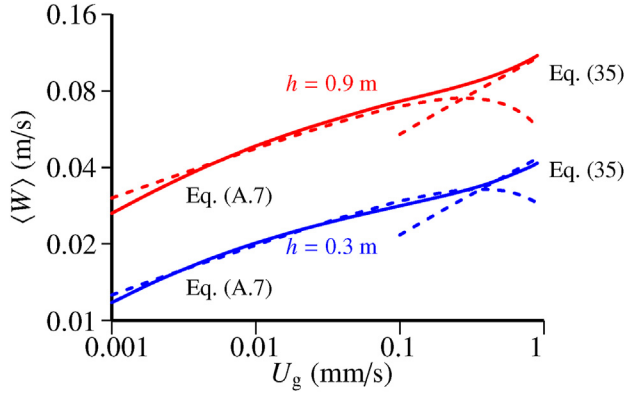


**Fig. 8 – Log-log plot of the flow rate ⟨W⟩ with $U_g$ for the properties listed in Table 1. For the step-function gas fraction profile, Eq. (35) valid at high $U_g$, we used $z_{eff} = 0.4h$ for $l = 10$ mm as indicated by Fig. D.11(a). For the exponential gas fraction profile, Eq. (A.7) valid at small $U_g$, we used $z_{eff} = 0.75h$ for $l = 10$ mm as indicated by Fig. D.11(b). It can be seen that the analytical results (dashed line) predict the flow rate with good accuracy.**

**Table 2 – Comparison of analytical results with numerical results obtained using COMSOL for $U_g = 0.2$ mm/s at $z = 900$ mm for a bubble diameter of 50 μm and properties used in Table 1.**

| | Numerical | | | Analytical | | | Difference | | |
|---|---|---|---|---|---|---|---|---|---|
| $\varepsilon_0$ | $\mathcal{W}$ (m/s) | $\delta_g$ (mm) | $w'$ (1/s) | $\mathcal{W}$ (mm) | $\delta_g$ (mm) | $w'$ (1/s) | $\mathcal{W}$ | $\delta_g$ | $w'$ |
| 0.3 | 1.88 | 1.11 | 1693.8 | 1.73 | 1.3 | 1324.5 | −8% | 17% | −22% |
| 0.4 | 1.61 | 0.92 | 1744.9 | 1.48 | 1.06 | 1393.6 | −8% | 15% | −20% |
| 0.5 | 1.39 | 0.82 | 1696.1 | 1.29 | 0.93 | 1389.9 | −8% | 13% | −18% |

## Conclusions

In this paper, we provide analytical relations for the velocity and gas fraction profile near a gas-evolving electrode. We derived analytical expressions for quantities like flow rate and wall shear rate for natural convection conditions. These relations are derived using the integral method, assuming first an exponentially shaped gas fraction profile and then a step-function gas fraction profile with constant electrode surface gas fraction and gas flux.

As we did not use any horizontal gas transport equation in our derivation, our analytical expressions for the step-function gas fraction profile are generally valid, for any type of horizontal transport mechanism.

We found that the characteristic liquid velocity $\mathcal{W}$ and the gas plume thickness $\delta_g$ increase as a function of height z for both exponential ($\delta_g \propto z^{1/5}$, $\mathcal{W} \propto z^{3/5}$) and step-function ($\delta_g \propto z^{1/3} - z^{0.43}$, $\mathcal{W} \propto z^{2/3} - z^{0.79}$) gas fraction profiles. The exact power depends on the value of $q = \delta_f/\delta_g$, which in case of a step-function gas fraction profile depends on the gas flux and maximum gas fraction through Eq. (26). The characteristic liquid velocity also increases with an increase in gas flux $U_g$. However, with an increase in gas flux, the gas plume thickness decreases for an exponential gas fraction profile as $U_g^{-1/5}$, while it increases for a step-function gas fraction profile as $U_g^{1/3} - U_g^{0.73}$ according to Eq. (28). We also observed that at a given height, the velocity profiles all cross at the same point for different high current densities. This is because while the plume thickness increases, $q$ decreases, so $\delta_f$ is almost a constant. Finally, we derived an analytical expression for the average superficial liquid velocity due to natural convection, Eq. (35), and validated it numerically for large current densities.

Both the exponential and step-function gas fraction profiles are relevant for water electrolyzers. Small bubbles at atmospheric pressure reach their maximum gas fraction quickly and develop a step-function gas fraction profile, while at high pressures, small heights, and/or relatively large bubbles, the gas fraction profile will be approximately exponential in shape.

## Declaration of competing interest

The authors declare that they have no known competing financial interests or personal relationships that could have appeared to influence the work reported in this paper.

## Appendix A. Exponential gas fraction profile

In section 3.1, we provided analytical relations for an exponential-shaped gas fraction profile of Eq. (7). Here we provide the derivation of the provided analytical expressions. At $x = 0$, the no-slip condition gives $u = w = 0$. In our derivation, we will neglect $\varepsilon \ll 1$ in comparison to unity, so $\nu_m = \nu$ and $\frac{\mathbf{u}_{Hd}}{1-\varepsilon/\varepsilon_{max}} \approx \mathbf{u}_{Hd}$. Using this, we can integrate Eq. (4) from $x = 0$ to $l$ with an exponential plume for $\delta_g \ll l$ to give

$$\mathcal{W} = \frac{\varepsilon_0 g \delta_g^2 q}{\nu(q+2)}. \tag{A.1}$$

The conservation of gas volume in Eq. (1) can be rewritten as

$$U_g z = H(q)\delta_g \varepsilon_0 \mathcal{W}. \tag{A.2}$$

Eq. (6) gives $\mathbf{u}_s \approx \mathbf{u}_{St} + \mathbf{u}_{Hd}$, so $u|_{x=0} \approx u_{Hd} \approx D_b/\delta_g$. For $\varepsilon_0 \ll 1$, we can rewrite Eq. (3) as

$$\frac{D_b \varepsilon_0}{\delta_g} = U_g. \tag{A.3}$$

Substituting Eq. (7), Eq. (8) and Eq. (A.1) in Eq. (4) and integrating between $x = 0$ and $x = l$ for $\delta_g \ll l$ gives

$$\frac{2\nu\mathcal{W}}{\delta_g q} = \frac{d(F(q)\delta_g \mathcal{W}^2)}{dz}, \tag{A.4}$$

where $F(q) \equiv \frac{432e^{-q} - 27e^{-2q} + 36q^3 - 162q^2 + 378q - 405}{108q^2}$. Eqs. (A.1)-(A.4) allow solutions in terms of powers of z. Eliminating $\varepsilon_0$ from Eqs. (A.1) and (A.2) using (A.3) gives

$$\mathcal{W} = \frac{U_g g \delta_g^3 q}{\nu D_b (q+2)} \quad \text{and} \quad D_b z = H(q)\delta_g^2 \mathcal{W}. \tag{A.5}$$

Eliminating $\mathcal{W}$ from Eq. (A.5), $\delta_g$ can be calculated by Eq. (10). Using (10) in Eq. (A.5) and (A.3), we can find $\mathcal{W}$ and $\varepsilon_0$ using Eqs. (11) and (12), respectively.

The exponential gas fraction profile will be relevant when the inlet gas flux $U_g$ is small. The transition to step-function profile occurs when $\varepsilon_0 \sim \varepsilon_{max}$. We can calculate the approximate condition for the transition in terms of gas flux using Eq. (12) as

$$U_g \approx \left(\frac{D_b^3 \varepsilon_{max}^5 g q H(q)}{\nu z (q+2)}\right)^{1/4}, \tag{A.6}$$

which gives $U_g \approx 0.08$ mm/s for the properties listed in Table 1. We see in Fig. 7 that the transition to block plume indeed starts around this value.

We can estimate the superficial liquid velocity or the liquid flow rate per unit flow area, $\langle W\rangle = \frac{1}{l}\int_0^l w(1-\varepsilon)dx$, using Eqs. (7) and (8) to be

$$\langle W\rangle = \frac{\mathcal{W}\delta_g(1-q+0.5q^2-e^{-q})}{ql}. \tag{A.7}$$

This expression should be evaluated at an effective height $z = z_{eff}$ for which the average liquid flow rate beyond $x = \delta_f$ is zero, which is further analyzed in Appendix D.

In thermal and solutal natural convection, Eq. (8) is often replaced by [30,81]:

$$w = \mathcal{W}e^{-\frac{x}{\delta_f}}\left(1-e^{-x/\delta_g}\right), \tag{A.8}$$

which gives

$$\begin{aligned}\delta_g &= \left(\frac{\nu D_b^2 z}{gU_g}\frac{(q+1)(q+2)(2q+1)}{q^3}\right)^{1/5},\\ \varepsilon_0 &= \left(\frac{\nu U_g^4 z}{gD_b^3}\frac{(q+1)(q+2)(2q+1)}{q^3}\right)^{1/5},\\ \mathcal{W} &= \left(\frac{D_b g^2 U_g^2 z^3}{\nu^2}\frac{(q+1)^2(2q+1)^2}{q^4}\right)^{1/5},\end{aligned} \tag{A.9}$$

These expressions have the same powers of z and $U_g$ as Eqs. 10–12, but depend differently on $q$. $q$, in this case, is given by

$$q \approx \sqrt{\frac{40\mathrm{Pr}_b}{7}}\frac{1+\sqrt{\mathrm{Pr}_b}}{1+2\sqrt{\mathrm{Pr}_b}}. \tag{A.10}$$

### *Bubble Prandtl Number*

The analytical relations derived for the exponential-shaped gas fraction profile require an estimate for $q$. Assuming that functions of $q$ can be expressed as some power of $q$ and comparing powers, we find from Eq. (A.1)-(A.4) that $q \propto z^0$. Eq. (A.4) can be written as

$$F(q)\frac{d(\delta_g\mathcal{W}^2)}{dz} = \frac{2\nu\mathcal{W}}{q\delta_g}. \tag{A.11}$$

Differentiating Eq. (A.2) with respect to z and using the expression in Eq. (1) gives

$$H(q)\frac{d(\delta_g\varepsilon_0\mathcal{W})}{dz} = U_g. \tag{A.12}$$

Dividing Eq. (A.11) by Eq. (A.12) using Eq. (A.3), we get

$$\frac{F(q)}{H(q)}\frac{\frac{d}{dz}(\delta_g\mathcal{W}^2)}{\frac{d}{dz}(\delta_g\varepsilon_0\mathcal{W})} = \frac{2\nu\mathcal{W}}{qD_b\varepsilon_0}. \tag{A.13}$$

Using the scalings $\mathcal{W}\propto z^{3/5}$, $\delta \propto z^{1/5}$ and $\varepsilon_0 \propto z^{1/5}$ in Eq. (A.13) gives

$$\mathrm{Pr}_b = \frac{\nu}{D_b} = \frac{7}{10}\frac{qF(q)}{H(q)}. \tag{A.14}$$

Equation (A.14) can be solved for $q$ for a given bubble Prandtl number. An excellent approximation for all values of $q$ with a relative error $<5\%$ is given by Eq. (14).

## Appendix B. Verification of boundary conditions

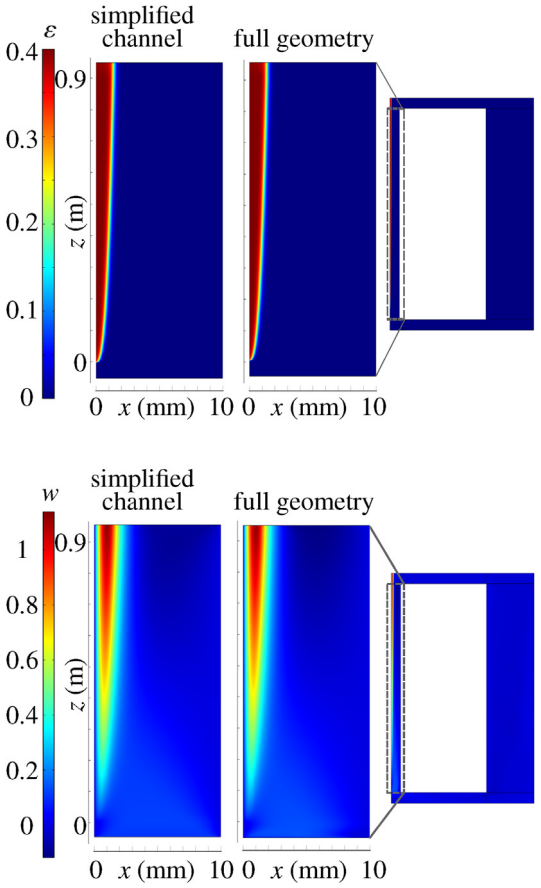


**Figure B.9 – Comparison of numerical results for (left) the simplified channel geometry used in the main text and (right) the full recirculating channel geometry. The results are shown for the properties listed in Table 1 at a superficial gas flux of $U_g = 0.5$ mm/s. We see that both (top) the gas fraction and (bottom) the vertical velocity are similar in both cases. This shows that the boundary conditions of Fig. 1 are appropriate to model the natural recirculation due to the gas produced at the vertical electrode. We have resized the recirculating geometry and the boxed region is zoomed to show the comparison with the simplified channel geometry.**

In this section, we verify the boundary conditions discussed in the main text and shown in the left part of Fig. 1 using a simulation of a full recirculation geometry including the downcomer section shown on the right of Fig. 1. For the full recirculation geometry, we use the same inlet boundary condition for the electrode, such that the gas flux is equal to $U_g$. At the top, we use a dispersed phase outlet boundary condition, so the gas escapes from the top boundary. For the electrolyte, a slip boundary condition is used at the top boundary. At other walls, a no-slip boundary condition is imposed. From Fig. B.9, we see that the results for the channel geometry used in the main text are similar to the full recirculating channel results, both for the gas fraction and the velocity profile with very minute differences near the top and the bottom of the channel, due to the boundary conditions. Owing to the better convergence and reduced simulation time, we used the channel geometry with the boundary conditions highlighted in Fig. 1.

## Appendix C. Expressions in the limit q→1

In this section, we derive Eqs. (31), (33) and (34). For the limit $q \to 1$, the last approximation of Eq. (27) is given as

$$q = \left(\frac{g\varepsilon_0\nu_m^2\bar{z}_c}{zU_g^4}\right)^{(1-\varepsilon_0)^4/7} \tag{C.1}$$

where the power 0.12 correspond to $\varepsilon_0 = 0.4$ and may vary slightly between 0.11 and 0.14 for a different $\varepsilon_0$.

To derive the scaling in the limit $q \to 1$ for $\delta_g$, $U_g$ and $w'$, we first need to locally write $\frac{q+2}{qh(q)}$, $\frac{q}{(q+2)h(q)^2}$ and $\frac{q^2}{(q+2)^2h(q)}$ appearing in Eqs. (28), (29) and (32) as powers of $q$ as

$$\left(\frac{q+2}{qh(q)}\right)^{1/3} = 2.83q^{a_1}, \quad \left(\frac{q}{(q+2)h(q)^2}\right)^{1/3} = 2.67q^{a_2}$$
$$\left(\frac{q^2}{(q+2)^2h(q)}\right)^{1/3} = 0.94q^{a_3} \tag{C.2}$$

where $a_1 = \frac{\ln\left(\frac{q+2}{2.83^3qh(q)}\right)}{3\ln(q)}$, $a_2 = \frac{\ln\left(\frac{q}{2.67^3(q+2)h(q)^2}\right)}{3\ln(q)}$ and $a_3 = \frac{\ln\left(\frac{q^2}{0.94^3(q+2)^2h(q)}\right)}{3\ln(q)}$.

In Fig. C.10, we plot the powers $a_1$, $a_2$ and $a_3$ as a function of $q$. We observe that $a_1$ and $a_2$ show a monotonous behavior with a finite negative value at $q = 1$ decreasing to nearly 0 at large $q$. In this case, both $\delta_g$ and $\mathcal{W}$ increase as $\bar{z}$ increases. Interestingly, $a_3$ increases from −0.1 to 0.13 for $q = 1 - 5$ and then decreases to 0 as $q$ approaches infinity. In this case, we would have a local minimum in the power of $U_g$ and z in the expression of $w'$. This minimum occurs when $q \sim 5$.

We can, using $a_1 = -0.8$, $a_2 = -0.95$ and $a_3 = -0.15$ and Eq. (C.1) and (C.2), write for the limit $q \to 1$:

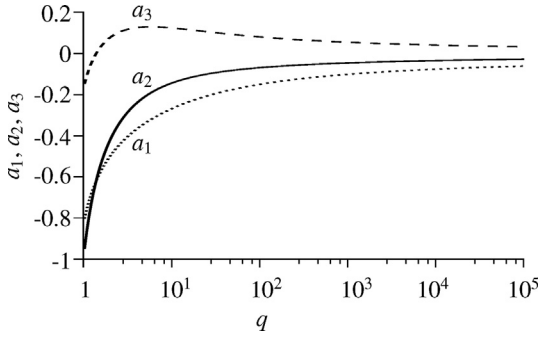


**Figure C.10 – Semi-log plot showing the variation of powers $a_1$, $a_2$, and $a_3$ with $q$. We observe that $a_1$ and $a_2$ change monotonously with $q$, while $a_3$ has a maxima near $q \sim 5$.**

$$\delta_g = 2.83\left(\frac{zU_g^4}{g\varepsilon_0^5\nu_m^2\bar{z}_c}\right)^{0.114(1-\varepsilon_0)^{1/4}}\left(\frac{\nu_m U_g z}{g\varepsilon_0^2}\right)^{1/3},$$
$$\mathcal{W} = 2.67\left(\frac{zU_g^4}{g\varepsilon_0^5\nu_m^2\bar{z}_c}\right)^{0.136(1-\varepsilon_0)^{1/4}}\left(\frac{gU_g^2z^2}{\nu_m\varepsilon_0}\right)^{1/3}, \quad \text{and}$$
$$w' = 0.94\left(\frac{zU_g^4}{g\varepsilon_0^5\nu_m^2\bar{z}_c}\right)^{0.021(1-\varepsilon_0)^{1/4}}\left(\frac{g^2U_gz\varepsilon_0}{\nu_m^2}\right)^{1/3}. \tag{C.3}$$

which on simplification gives Eqs. (31) and (33). Similarly, the local minima in the powers of $U_g$ and z in the expression of $w'$ is obtained by using $a_3 = 0.13$ near $q \to 5$ in Eq. (C.1) and (C.2) to give

$$w' = 0.94\left(\frac{g\varepsilon_0\nu_m^2\bar{z}_c}{zU_g^4}\right)^{0.019(1-\varepsilon_0)^{1/4}}\left(\frac{g^2U_gz\varepsilon_0}{\nu_m^2}\right)^{1/3}. \tag{C.4}$$

resulting in Eq. (34) upon simplification and using $\varepsilon_0 = 0.4$.

### *Appendix D. The effective height z_eff*

In the main text, we used an effective height $z_{eff}$ for which the average velocity between $\delta_f < x < l$ is negligible in simulations. In this section, we will try to quantify this height with the help of our simulations. To do this, we performed various simulations varying the current density, electrode height, channel width, and bubble diameter. In Fig. D.11, we show the results of various simulations varying different parameters and find that the $z_{eff}$ becomes approximately independent of the channel width for wide channels of a few cm in case of a step-function plume and a bit more in case of an exponential plume. There is some variation with bubble size, height in case of an exponential plume, and maximum gas fraction in case of a step-function plume. Except for thin channels, as a

rough approximation one may take $z_{eff}$ ~ $h$/3 for a step-function plume and $h$/2 for an exponential plume.

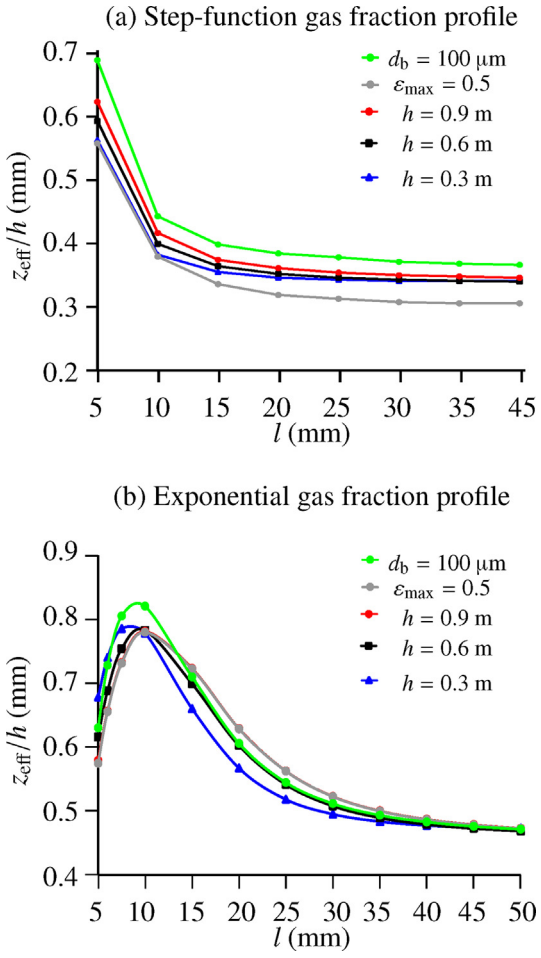


**Figure D.11 – Plot showing $z_{eff}/h$ as a function of gap width for different electrolyzer heights, maximum gas fraction, and bubble diameter. Here $z_{eff}$ is the height for which the average superficial velocities for the analytical and numerical results are the same. Unless otherwise mentioned, the properties listed in Table 1 are used. These results for a step-function gas fraction profile ($U_g = 1$ mm/s) show that $z_{eff}/h$ becomes independent of gap width $l$, but depends somewhat on $d_b$ and $\varepsilon_{max}$. The results for the exponential gas fraction profile ($U_g = 0.01$ mm/s) seem to indicate that a large variation in $z_{eff}/h$ becomes independent of $l$ for a bit larger values. For the exponential case, the red and gray lines overlap as the gas fraction remains small, and the maximum gas fraction has no effect on the hydrodynamics.**

## REFERENCES


[1] Perron AL, Kiss LI, Poncsák S. J Appl Electrochem 2007;37:303–10.
[2] Boissonneau P, Byrne P. J Appl Electrochem 2000;30:767–75.
[3] Karlsson RKB, Cornell A. Chem Rev 2016;116:2982–3028.
[4] Byrne P, Bosander P, Parhammar O, Fontes E. J Appl Electrochem 2000;30:1361–7.
[5] Zeng K, Zhang D. Prog Energy Combust Sci 2010;36:307–26.
[6] Vogt H. J Appl Electrochem 1999;29:1155–9.
[7] Bongenaar-Schlenter BE, Janssen LJJ, Van Stralen SJD, Barendrecht E. J Appl Electrochem 1985;15:537–48.
[8] Schalenbach M, Lueke W, Stolten D. J Electrochem Soc 2016;163:F1480.
[9] Rajora A, Haverkort JW. Chem Eng Sci 2022;260:117823.
[10] Haverkort JW, Rajaei H. J Power Sources 2021;497:229864.
[11] Rajaei H, Rajora A, Haverkort JW. J Power Sources 2021;491:229364.
[12] Sigrist L, Dossenbach O, Ibl N. J Appl Electrochem 1980;10:223–8.
[13] Bakker MM, Vermaas DA. Electrochim Acta 2019;319:148–57.
[14] Janssen LJJ. J Appl Electrochem 2000;30:507–9.
[15] Angulo A, van der Linde P, Gardeniers H, Modestino M, Rivas DF. Joule 2020;4:555–79.
[16] Gabrielli C, Huet F, Keddam M, Macias A, Sahar A. J Appl Electrochem 1989;19:617–29.
[17] Iwata R, Zhang L, Wilke KL, Gong S, He M, Gallant BM, Wang EN. Joule 2021;5:887–900.
[18] Vogt H. J Appl Electrochem 1983;13:87–8.
[19] Dukovic J, Tobias CW. J Electrochem Soc 1987;134:331.
[20] Lee JK, Bazylak A. Joule 2021;5:19–21.
[21] Vogt H. Electrochim Acta 1987;32:633–6.
[22] Obata K, Abdi F. Sustainable energy & fuels. 2021.
[23] Babu R, Das MK. Int J Hydrogen Energy 2019;44:14467–80.
[24] Mandin P, Wüthrich R, Roustan H. Computer aided chemical engineering, vol. 27. Elsevier; 2009. p. 435–40.
[25] Wang M, Wang Z, Gong X, Guo Z. Renew Sustain Energy Rev 2014;29:573–88.
[26] Hreiz R, Abdelouahed L, Fuenfschilling D, Lapicque F. Chem Eng Res Des 2015;100:268–81.
[27] Tobias C, Eisenberg M, Wilke C. J Electrochem Soc 1952;99:359C.
[28] Ibl N, Müller R. J Electrochem Soc 1958;105:346.
[29] Janssen LJJ. J Appl Electrochem 1987;17:1177–89.
[30] Bejan A. Convection heat transfer. John Wiley & sons; 2013.
[31] Sparrow EM, Gregg J. Trans Am Soc Mech Eng 1956;78:435–40.
[32] Capobianchi M, Aziz A. Int J Therm Sci 2012;54:82–8.
[33] Guha A, Pradhan K. Int J Therm Sci 2017;111:475–90.
[34] O'Neil GD, Christian CD, Brown DE, Esposito DV. J Electrochem Soc 2016;163:F3012.
[35] Gillespie MI, Van Der Merwe F, Kriek RJ. J Power Sources 2015;293:228–35.
[36] Esposito DV. Joule 2017;1:651–8.
[37] Obata K, Mokeddem A, Abdi FF. Cell Reports Physical Science 2021:100358.
[38] Hashemi SMH, Modestino MA, Psaltis D. Energy Environ Sci 2015;8:2003–9.
[39] Davis JT, Qi J, Fan X, Bui JC, Esposito DV. Int J Hydrogen Energy 2018;43:1224–38.
[40] Pang X, Davis JT, Harvey AD, Esposito DV. Energy Environ Sci 2020;13:3663–78.
[41] Phillips R, Dunnill CW. RSC Adv 2016;6:100643–51.
[42] Jupudi RS, Zhang H, Zappi G, Bourgeois R. J Comput Multiph Flows 2009;1:341–7.
[43] Wong XY, Zhuo Y, Shen Y. Ind Eng Chem Res 2021;60:12429–46.
[44] Swiegers GF, Terrett RN, Tsekouras G, Tsuzuki T, Pace RJ, Stranger R. Sustain Energy Fuels 2021;5:1280–310.
[45] Riviere N, Cartellier A. Eur J Mech B Fluid 1999;18:823–46.
[46] Schillings J, Doche O, Deseure J. Int J Heat Mass Tran 2015;85:292–9.
[47] Vogt H. J Appl Electrochem 1982;12:261–6.
[48] Gebhart B, Jaluria Y, Mahajan RL, Sammakia B. Buoyancy-induced flows and transport. New York, NY (USA): Hemisphere Publishing; 1988.
[49] Ishii M. NASA sti/recon technical report. A 1975;75:29657.

[50] Wedin R, Dahlkild AA. Ind Eng Chem Res 2001;40:5228–33.
[51] Vogt H. Electrochim Acta 2011;56:2404–10.
[52] Raman A, Peñas P, van der Meer D, Lohse D, Gardeniers H, Fernández Rivas D. Electrochim Acta 2022;425:140691.
[53] Ishii M, Zuber N. AIChE J 1979;25:843–55.
[54] Jamshidi R, Angeli P, Mazzei L. Phys Fluids 2019;31:013302.
[55] Krikke IRC. Modeling the effect of dissolved gas on the bubble layer along a vertical gas evolving electrode. The Netherlands: Master's thesis, Delft University of Technology; 2021.
[56] Schiller L. Z. Vereines Deutscher Inge. 1933;77:318–21.
[57] Crowe C, Sommerfeld M, Tsuji Y, et al. Multiphase flows with. Ż; 1998.
[58] Clift R, Grace JR, Weber ME. Bubbles, drops, and particles. Courier Corporation; 2005.
[59] Nicolai H, Herzhaft B, Hinch EJ, Oger L, Guazzelli E. Phys Fluids 1995;7:12–23.
[60] T. Hales, M. Adams, G. Bauer, T. D. Dang, J. Harrison, H. Le Truong, C. Kaliszyk, V. Magron, S. McLaughlin, T. T. Nguyen, et al., in: Forum of mathematics, pi, volume vol. 5, Cambridge University Press.
[61] Scott GD. Nature 1960;188:908–9.
[62] Wang Z, Pereira J-M, Gan Y. Powder Technol 2021;378:60–4.
[63] Kreysa G, Kuhn M. J Appl Electrochem 1985;15:517–26.
[64] De Strycker Y. A bubble curtain model applied in chlorate electrolysis, Master's thesis. Chalmers University of Technology; 2012.
[65] Haug P, Kreitz B, Koj M, Turek T. Int J Hydrogen Energy 2017;42:15689–707.
[66] Coenen ELJ, Janssen LJJ. J Appl Electrochem 1997;27:1143–8.
[67] Colli AN, Bisang JM. J Electrochem Soc 2022;169:034524.
[68] Vogt H. J Appl Electrochem 1987;17:419–26.
[69] Johnson PC, Jackson R. J Fluid Mech 1987;176:67–93.
[70] Josserand C, Lagrée P-Y, Lhuillier D. EPL 2005;73:363.
[71] Cheng Z, Hsu T-J, Calantoni J. Coast Eng 2017;119:32–50.
[72] Si P, Shi H, Yu X. Landslides 2019;16:485–96.
[73] Tiwari P, Antal SP, Podowski MZ. Comput Fluids 2009;38:727–37.
[74] Matsushima H, Fukunaka Y, Kuribayashi K. Electrochim Acta 2006;51:4190–8.
[75] Fukunaka Y, Suzuki K, Ueda A, Kondo Y. J Electrochem Soc 1989;136:1002.
[76] CFD Module User's guide v5.6. COMSOL; 2020.
[77] Desrayaud G, Chénier E, Joulin A, Bastide A, Brangeon B, Caltagirone J, Cherif Y, Eymard R, Garnier C, Giroux-Julien S, et al. Int J Therm Sci 2013;72:18–33.
[78] Sun H, Li R, Chénier E, Lauriat G. Heat Mass Tran 2012;48:1125–34.
[79] Brangeon B, Joubert P, Bastide A. Int J Therm Sci 2015;95:64–72.
[80] Hiraoka S, Yamada I, Mori H, Sugimoto H, Hakushi N, Matsuura A, Nakamura H. Electrochim Acta 1986;31:349–54.
[81] Faghri A, Zhang Y, Howell JR. Advanced heat and mass transfer. Global Digital Press; 2010.